Fictitious Particle Method: A Numerical Model for Flows Including Dense Solids with Large Size Difference

Takuya Tsuji, Kyohei Higashida, Yoshitomo Okuyama, and Toshitsugu Tanaka
Dept. of Mechanical Engineering, Osaka University, 2-1 Yamadaoka Suita, Osaka, Japan

DOI 10.1002/aic.14355
Published online February 4, 2014 in Wiley Online Library (wileyonlinelibrary.com)

Large solids coexist with small solids in a number of dense gas-solid flow applications such as fluidized beds and pneumatic conveyers. A new numerical model that is based on the discrete element method–computational fluid dynamics mesoscopic model and extended by introducing an idea appearing in volume penalization method is presented. In computational cells including large and small solids, the amount of momentum exchange between the fluid and the solids is estimated by assuming that a large solid consist of small, dense fictitious particles. We describe the proposed model in detail and show the optimal model parameters found through a number of parameter-dependency studies. Validation study is performed for the motion of a large sphere in a bubbling fluidized bed and good agreements are confirmed for floating and sinking motions of the sphere between the present model and the experiment. © 2014 American Institute of Chemical Engineers *AIChE J*, 60: 1606–1620, 2014

Keywords: fluidization, computational fluid dynamics, particle technology, multiphase flow

Introduction

In practical flow applications including dense solids such as fluidized beds and pneumatic conveyers, the size of solid materials is not uniform and large solids coexist with small solids. In coal and wooden biomass gasification processes using bubbling fluidized beds, for instance, sand particles of O ($10^{-5}-10^{-4}$ m) exist in the bed in addition to coal and biomass fuel particles of O (10^{-3} m), enhancing fluidization and heat transfer. The size ratio between these two solids is O (10–100). The large size difference induces characteristic motions of solids and significantly influences the mixing and segregation characteristics of the beds. Additionally, in industrial continuous systems, residence time of fuel particles in the equipment is important for system efficiency. The large size difference influences the floating and sinking motions of the fuel particles and the residence time. The large size difference of solids is also observed and important in a number of other applications, such as dry specific separation,[1,2] heat treatment,[3] and granulation.[4]

A number of numerical models have been developed for flows including dense solids. The discrete element method–computational fluid dynamics (DEM–CFD) mesoscopic model,[5,6] one of Eulerian–Lagrangian approaches, has been widely used. As its extension, DEM–CFD models for binary and polydisperse systems have been proposed, while the size-ratio of solids in these models is as high as four.[7–12] In DEM–CFD, computational cells for fluid calculation must, at the same time, be both sufficiently small compared to the size of the mesoscopic characteristic structures such as bubbles and sufficiently large compared to the size of emulsion particles. If the size of large solids is not small enough compared to the mesoscopic structures induced by small solids and exceeds the computational cell size for fluid calculation, it is difficult to simulate the flow with conventional DEM–CFD models.

The influence of large solid objects immersed in dense gas-solid flows has been a subject of study and a number of numerical models have been proposed. Rong et al.[13] investigated the influence of cylinders fixed in a bubbling fluidized bed. The geometry of cylinders was properly represented in contact calculations using DEM; however, it was replaced by nonsmooth stepwise boundaries on a Cartesian grid in CFD calculations. Wu et al.[14] and Liu et al.[15] also performed simulations of a bubbling fluidized bed with an immersed tube. Unstructured grids fitted to the immersed tube were used in their studies. Guo et al.[16] combined an immersed boundary method (IBM) with a DEM–CFD model. By virtue of IBM, it is possible to calculate moving objects using a fixed Cartesian grid in their model and it was applied to a number of problems including a gas-fluidized bed with a vibrating tube. The combination of IBM and DEM–CFD model was also proposed by Takeuchi et al.[17] Dietiker et al.[18] recently introduced a cut-cell technique to an open source multiphase flow solver. They applied their method to two and three-dimensional bubbling fluidized beds with a bank of 25 submerged tubes.

The purpose of this study is to develop a numerical model capable of predicting and reproducing the motion of flows including dense solids with large size differences, which are difficult to treat using the conventional DEM–CFD models, in a simple and efficient manner. In DEM–CFD, the momentum exchange between solid and fluid phases at each computational cell is obtained using empirical drag correlations.

Correspondence concerning this article should be addressed to T. Tsuji at tak@mech.eng.osaka-u.ac.jp.

When a solid that is large in comparison to the size of computational cells is introduced, it is necessary to express the momentum exchange between the large solid and surrounding fluid. Our proposed model is based on the DEM–CFD mesoscopic model, but it is extended by introducing an idea that appeared in the Volume penalization (VP) method[19,20] one of methods for the resolved direct numerical simulation of solid–fluid systems.

In the following sections, we use a binary system consisting of small and large solids to simplify our explanations. Both solids are spherical and, hereafter, these are referred to as *particle* and *sphere*, respectively. Additionally, we assume that the particle and sphere are, respectively, smaller and larger than the computational cell used for fluid calculation, as shown in Figure 1.

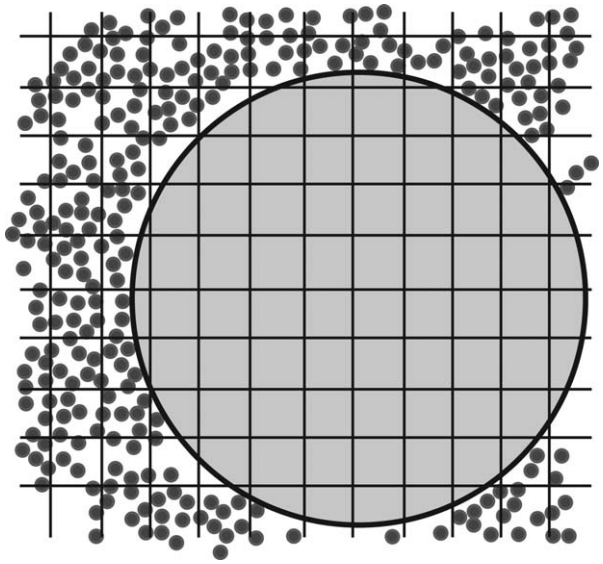

Figure 1. Size relation among computational cells, particles, and sphere.

Governing Equations and Proposed Model

Governing equations of fluid motion in DEM–CFD mesoscopic model

In the DEM–CFD mesoscopic model,[5] fluid motion is expressed by the following incompressible continuity and momentum equation for locally phase-averaged quantities[21]:

$$\frac{\partial}{\partial t}\varepsilon+\nabla\cdot(\varepsilon\boldsymbol{u})=0 \tag{1}$$

$$\frac{\partial}{\partial t}(\varepsilon\boldsymbol{u})+\nabla\cdot(\varepsilon\boldsymbol{u}\boldsymbol{u})=-\frac{\varepsilon}{\rho_{\mathrm{f}}}\nabla p+\varepsilon\nu\nabla^2\boldsymbol{u}+\boldsymbol{f} \tag{2}$$

where ε is the void fraction in a computational cell, and $\boldsymbol{u}$ and p are the locally phase-averaged fluid velocity and pressure, respectively. The density of the fluid is ρ_{f} and ν is the kinematic viscosity. The momentum exchange between the fluid and particles is denoted by $\boldsymbol{f}$, which is given by the following equation:

$$\boldsymbol{f}=\frac{\beta}{\rho_{\mathrm{f}}}(\bar{\boldsymbol{U}}-\boldsymbol{u}) \tag{3}$$

where β is the drag coefficient due to the existence of particles, usually obtained using empirical correlations.

Volume penalization method

The VP method[19,20] is one of the resolved direct numerical simulation techniques for the interaction between a fluid and solid body. In this method, computational cells should be smaller than solid bodies existing in the flow field. In the VP approach, a flow is considered in a unified domain including both fluid and solid phases. The method is based on the idea of modeling the solid body as a porous media; the momentum equation is expressed as follows

$$\frac{\partial\boldsymbol{u}_\eta}{\partial t}+\nabla\cdot\left(\boldsymbol{u}_\eta\boldsymbol{u}_\eta\right)=-\frac{1}{\rho_{\mathrm{f}}}\nabla p_\eta+\nu\nabla^2\boldsymbol{u}_\eta+\boldsymbol{f}_\eta \tag{4}$$

$\boldsymbol{u}_\eta$ and p_η denote the velocity and pressure of the fluid, respectively, and $\boldsymbol{f}_\eta$ is the penalization term given by

$$\boldsymbol{f}_\eta=\frac{\chi_\Omega}{\eta}\left(\boldsymbol{u}_{\mathrm{s}}-\boldsymbol{u}_\eta\right) \tag{5}$$

where $\boldsymbol{u}_{\mathrm{s}}$ is the velocity of the solid body. The mask function χ_Ω becomes unity when the cells are completely immersed in the solid body and vanishes in the fluid cells. The permeability η governs the penetration of fluid into the body, which is assumed to be porous. The penalization term works when $\chi_\Omega=1$ and a relative velocity exists between the fluid and solid body. With small η, the penetration of fluid flow is restricted and a solidification of the body is realized substantially.

It is interesting that the DEM–CFD and the VP method are common in that the existence of solids is represented by introducing fluid resistance forces that are proportional to the slip velocity and work against the relative motion between fluid and solid phases (Eqs. 2–5), although the spatial scales in which the two methods represent the flow field are different.

Proposed model: Fictitious particle method

In the system we considered, large spheres coexist with small particles. Hence, it is required to take into account the momentum exchanges between the spheres and fluid in addition to those between the particles and fluid. As aforementioned, we assume that the particles are small compared to the computational cells and the spheres are large, as shown in Figure 1. In the cells containing only particles, as shown in Figure 2a, which is a typical situation in the conventional DEM–CFD, the momentum exchange is obtained using Eq. 3. In the cells completely immersed in a sphere, as in Figure 2c, the VP method is applicable. However, for computational cells including both particles and spheres, as in Figure 2b, there is no general rule. Moreover, these three cases in Figure 2 are ubiquitous in practical flow fields, and it is preferred to treat the momentum exchange between fluid and solids including particles and spheres in a unified manner.

In this study, instead of porous media introduced in the VP method, we assume that each sphere consists of dense monosized fictitious small particles, when the momentum exchange is considered as shown in Figure 3b. The diameter of a fictitious particle d_{fic} and its solid volume fraction inside a sphere α_{fic}, which is called the *fictitious volume fraction*, are introduced as model parameters. It is generally known that a large fluid resistance is obtained for the flows including densely packed small particles. Hence, as in the VP method, in which the realization of solidity of immersed objects depends on the magnitude of permeability, we can

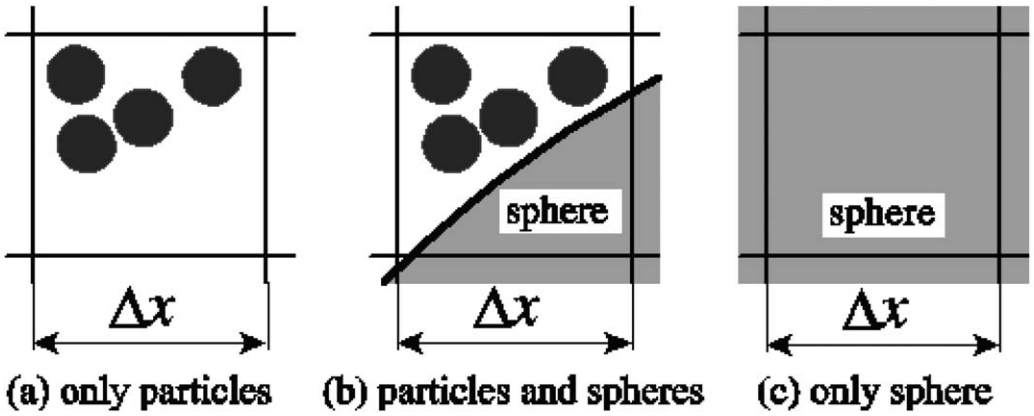

Figure 2. Computational cell including only particles, only sphere, and its mixtures.

expect that the solidity of a sphere expressed as an agglomerate of fictitious small particles is controllable using the values of d_{fic} and α_{fic} in the present model.

The same continuity and momentum equations as in the conventional DEM–CFD model, with the exception of the momentum exchange term, are used for fluid motion:

$$\frac{\partial}{\partial t}\varepsilon+\nabla\cdot(\varepsilon\boldsymbol{u})=0 \tag{6}$$

$$\frac{\partial}{\partial t}(\varepsilon\boldsymbol{u})+\nabla\cdot(\varepsilon\boldsymbol{u}\boldsymbol{u})=-\frac{\varepsilon}{\rho_f}\nabla p+\varepsilon\nu\nabla^2\boldsymbol{u}+\boldsymbol{f}_{\mathrm{FPM}} \tag{7}$$

By introducing the volume fraction of the particle α_{p} and sphere α_{s} in a computational cell, ε can be expressed as

$$\varepsilon=1-\alpha_{\mathrm{p}}-\alpha_{\mathrm{s}}\alpha_{\mathrm{fic}} \tag{8}$$

The momentum exchange term $\boldsymbol{f}_{\mathrm{FPM}}$ (FPM, fictitious particle method) is given by the following equation:

$$\boldsymbol{f}_{\mathrm{FPM}}=\frac{\beta_{\mathrm{FPM}}}{\rho_{\mathrm{f}}}\left(\overline{\boldsymbol{U}}_{\mathrm{FPM}}-\boldsymbol{u}\right) \tag{9}$$

where β_{FPM} is the drag coefficient. In this study, we assume a homogeneous binary mixture of particles with diameter d_{p} and fictitious particles with diameter d_{fic} in Figure 3c, as is usually assumed in conventional DEM–CFD models. We obtain β_{FPM} using the Ergun equation (Eq. 10)[22] and the Wen and Yu equation (Eq. 11)[23]:

$$\beta_{\mathrm{FPM}}=\begin{cases}\dfrac{\mu_{\mathrm{f}}(1-\varepsilon)}{\langle d_{\mathrm{FPM}}\rangle^2\varepsilon}\left[150(1-\varepsilon)+1.75\,Re\right] & (\varepsilon\le 0.8) \quad (10)\\[2ex] \dfrac{3}{4}C_{\mathrm{D}}\dfrac{\mu_{\mathrm{f}}(1-\varepsilon)}{\langle d_{\mathrm{FPM}}\rangle^2}\varepsilon^{-2.7}\,Re & (\varepsilon>0.8) \quad (11)\end{cases}$$

μ_{f} is the viscosity of the fluid and C_{D} is the drag coefficient of a particle. In Eq. 11, C_{D} is the drag coefficient of a single particle given by the Schiller and Naumann equation (Eq. 12)[24] and Newton's law of drag (Eq. 13):

$$C_{\mathrm{D}}=\begin{cases}24\left(1+0.15\,Re^{0.687}\right)/Re & (Re\le 1000) \quad (12)\\[2ex] 0.43 & (Re>1000) \quad (13)\end{cases}$$

The particle Reynolds number Re is defined as follows.

$$Re=\frac{|\bar{U}_{\mathrm{FPM}}-\boldsymbol{u}|\rho_{\mathrm{f}}\varepsilon\langle d_{\mathrm{FPM}}\rangle}{\mu_{\mathrm{f}}} \tag{14}$$

In Eqs. 9 and 14, $\overline{\boldsymbol{U}}_{\mathrm{FPM}}$ is the average velocity of all solids existing in a computational cell. It is obtained by the following volume-weighted form

$$\overline{\boldsymbol{U}}_{\mathrm{FPM}}=\frac{\alpha_{\mathrm{p}}\overline{\boldsymbol{U}}_{\mathrm{p}}+\alpha_{\mathrm{s}}\alpha_{\mathrm{fic}}\overline{\boldsymbol{U}}_{\mathrm{s}}}{1-\varepsilon} \tag{15}$$

where $\overline{\boldsymbol{U}}_{\mathrm{p}}$ is the average velocity of particles existing in the cell

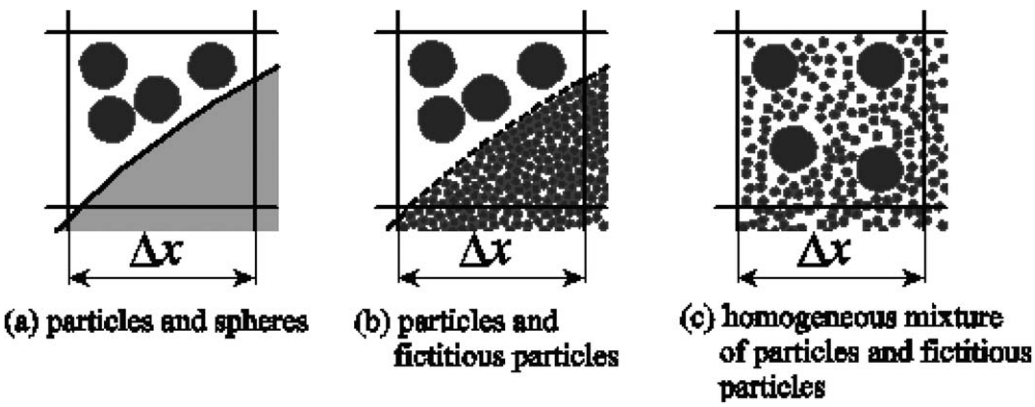

Figure 3. Modeling based on small fictitious particles.

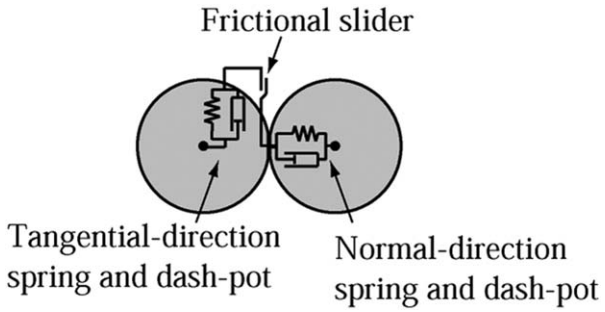

Figure 4. Contact force model.

$$\overline{\boldsymbol{U}}_{\mathrm{p}}=\frac{\sum_{i=1}^{N_{\mathrm{Cp}}}\boldsymbol{U}_{\mathrm{p}i}}{N_{\mathrm{p}}} \tag{16}$$

A number of spheres may exist in a flow field, and we can expect situations in which a cell includes the parts of neighboring multiple spheres. In this study, the average velocity of spheres in the cell $\overline{\boldsymbol{U}}_{\mathrm{s}}$ is given as

$$\overline{\boldsymbol{U}}_{\mathrm{s}}=\frac{\sum_{j=1}^{N_{\mathrm{Cs}}}\alpha_{\mathrm{s}j}\boldsymbol{U}_{\mathrm{s}j}}{\alpha_{\mathrm{s}}} \tag{17}$$

where $\alpha_{\mathrm{s}j}$ is the volume fraction of sphere j which satisfies the following relation.

$$\alpha_{\mathrm{s}}=\sum_{j=1}^{N_{\mathrm{Cs}}}\alpha_{\mathrm{s}j} \tag{18}$$

It is noted that $\overline{\boldsymbol{U}}_{\mathrm{s}}$ is defined according to the velocity of spheres as a solid body $\boldsymbol{U}_{\mathrm{s}j}$ and the velocity of fictitious particles never appears explicitly in the present model. In addition, $\alpha_{\mathrm{s}j}$ can be obtained from the geometrical relations between spheres and computational cells.

In Eqs. 10, 11, and 14, $<d_{\mathrm{FPM}}>$ shows the Sauter mean diameter in a cell containing both particles and spheres, which is given by

$$\langle d_{\mathrm{FPM}}\rangle=\frac{N_{\mathrm{Cp}}d_{\mathrm{p}}^3+N_{\mathrm{fic}}d_{\mathrm{fic}}^3}{N_{\mathrm{Cp}}d_{\mathrm{p}}^2+N_{\mathrm{fic}}d_{\mathrm{fic}}^2} \tag{19}$$

where N_{fic} is the estimated number of fictitious particles in the computational cell and d_{p} is the diameter of the particles. According to the volume of the computational cell V_{c}, N_{Cp} and N_{fic} can be expressed as Eqs. 20 and 21, respectively.

$$N_{\mathrm{Cp}}=\frac{6V_{\mathrm{c}}\alpha_{\mathrm{p}}}{\pi {d_{\mathrm{p}}}^3} \tag{20}$$

$$N_{\mathrm{fic}}=\frac{6V_{\mathrm{c}}\alpha_{\mathrm{s}}\alpha_{\mathrm{fic}}}{\pi {d_{\mathrm{fic}}}^3} \tag{21}$$

Substituting Eqs. 20 and 21 into Eq. 19, we obtain the following expression for $<d_{\mathrm{FPM}}>$.

$$\langle d_{\mathrm{FPM}}\rangle=\frac{1-\varepsilon}{\dfrac{\alpha_{\mathrm{p}}}{d_{\mathrm{p}}}+\dfrac{\alpha_{\mathrm{s}}\alpha_{\mathrm{fic}}}{d_{\mathrm{fic}}}} \tag{22}$$

We estimate the amount of momentum exchange between fluid and solids by assuming a sphere consists of fictitious small particles without actually replacing a sphere with small fictitious particles. Hence, excessive computer resources are not needed to represent each fictitious particle in the proposed model.

The proposed model is an Eulerian–Lagrangian approach, and the motion of the particles and spheres is obtained by solving the translational and rotational equations of motion simultaneously. As with the conventional DEM–CFD models, contact forces among particles, spheres, and walls are expressed using DEM consisting of a linear spring, dash-pot, and frictional slider, as shown in Figure 4.

The translational and rotational equations of motion for a particle i are expressed, respectively, as

$$m_{\mathrm{p}}\dot{\boldsymbol{U}}_{\mathrm{p}i}=\sum \boldsymbol{f}_{\mathrm{Cp}i}+\boldsymbol{f}_{\mathrm{Dp}i}+m_{\mathrm{p}}\boldsymbol{g} \tag{23}$$

$$I_{\mathrm{p}}\dot{\boldsymbol{\omega}}_{\mathrm{p}i}=\sum M_{\mathrm{p}i} \tag{24}$$

where m_{p} is the mass of the particle; $\boldsymbol{f}_{\mathrm{Cp}i}$ is the contact force acting on particle i from the other particles, spheres, and walls; and $\boldsymbol{f}_{\mathrm{Dp}i}$ is the fluid force acting on particle i. This is obtained as the summation of the viscous drag force, which is given as the counteraction of $\boldsymbol{f}_{\mathrm{FPM}}$ in Eq. 9 and the pressure gradient force:

$$\boldsymbol{f}_{\mathrm{Dp}i}=\frac{\beta_{\mathrm{FPM}}V_{\mathrm{p}}}{1-\varepsilon}\left(\boldsymbol{u}-\boldsymbol{U}_{\mathrm{p}i}\right)-\nabla pV_{\mathrm{p}} \tag{25}$$

where V_{p} is the volume of a particle, $\boldsymbol{g}$ is the gravity acceleration, I_{p} is the moment of inertia of a particle, and $\boldsymbol{M}_{\mathrm{p}i}$ is the torque acting on particle i due to the contacts with other particles, spheres, and walls.

The translational and rotational equations of motion of a sphere j are expressed as

$$m_{\mathrm{s}}\dot{\boldsymbol{U}}_{\mathrm{s}j}=\sum \boldsymbol{f}_{\mathrm{Cs}j}+\boldsymbol{f}_{\mathrm{Ds}j}+m_{\mathrm{s}}\boldsymbol{g} \tag{26}$$

$$I_{\mathrm{s}}\dot{\boldsymbol{\omega}}_{\mathrm{s}j}=\sum M_{\mathrm{s}j} \tag{27}$$

where m_{s} is the mass of a sphere; $\boldsymbol{f}_{\mathrm{Cs}j}$ is the contact force acting on sphere j from the particles, walls, and other spheres; and $\boldsymbol{f}_{\mathrm{Ds}j}$ is the fluid force acting on sphere j. Similar to the VP method,[19,20] it is obtained by integrating the fluid forces working on the sphere body as follows:

$$\boldsymbol{f}_{\mathrm{Ds}j}=\int_{V_s}\left\{\frac{\beta_{\mathrm{FPM}}\alpha_{\mathrm{fic}}}{1-\varepsilon}\left(\boldsymbol{u}-\boldsymbol{U}_{\mathrm{s}j}\right)-\alpha_{\mathrm{fic}}\nabla p\right\}dV \tag{28}$$

where V_{s} is the volume of sphere; $\boldsymbol{M}_{\mathrm{s}j}$ is the torque acting on sphere j because of contact with particles, wall, other spheres, and fluid; and I_{s} is the moment of inertia of a sphere.

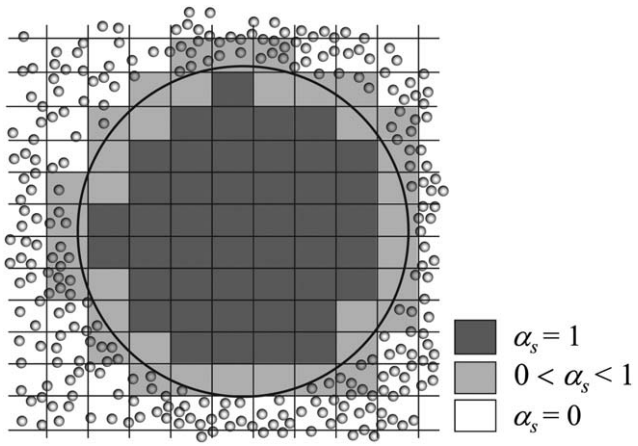

Figure 5. Cells classified by α_{s}.

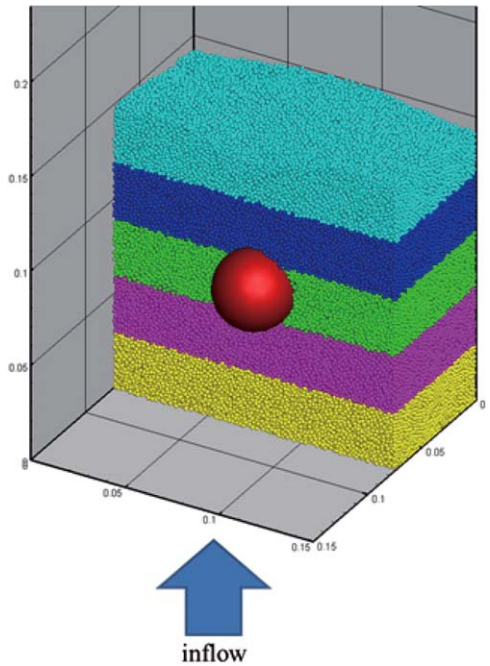

Figure 6. A sphere fixed in a packed bed (only particles in a half domain are shown).

[Color figure can be viewed in the online issue, which is available at wileyonlinelibrary.com.]

Discussion on Model Parameters

In this section, discussion is made for the model parameters, α_{fic} and d_{fic}, introduced in the former section.

The SIMPLE method is used to couple Eqs. 6 and 7. We use a second-order central difference scheme for spatial derivatives and a first-order upwind scheme for the convective term. We use the Euler method to establish temporal increments. The volume fraction of spheres at each computational cell is obtained by the subdivision volume counting method.[25] The numerical code is parallelized based on the domain decomposition technique.[26]

Model parameters for cells completely immersed in a sphere ($\alpha_s = 1$)

In the cells completely immersed in a sphere ($\alpha_s = 1$), shown with dark gray in Figure 5, the VP method is directly applicable. The solidity of an object is realized by choosing a small magnitude of permeability, and hence, large fluid resistance in the VP method. This small permeability corresponds to a large β_{FPM} in the proposed model framework. We know that it can be realized by choosing small d_{fic} and large α_{fic} from Eqs. 10 and 11; however, there is no need to directly control d_{fic} and α_{fic} for the cells with $\alpha_s = 1$ because only fictitious particles exist. Rather, it is straightforward and easy to control β_{FPM} directly. The next section will describe the model parameters adequate for the cells including both spheres and particles.

β_{FPM} at the cells with $\alpha_s = 1$ should be large enough to avoid the penetration of fluid into the sphere body. In this study, it is determined on the basis of the amount of fluid penetration and fluid force working on a large sphere fixed within a packed bed. The calculation domain is a rectangular box with dimensions of 0.15 m width, 0.15 m depth, and 0.60 m height. The x, y, and z axis represent width, depth, and height directions, respectively. The diameter of particles filling the domain and the sphere are 2.0×10^{-3} and 40.0×10^{-3} m, respectively. Hence, the sphere is 20 times larger than the particles. The sphere is fixed at $x = 0.075$, $y = 0.075$, and $z = 0.075$ m. The particles settle down from the top, and their positions are fixed after they become steady as shown in Figure 6. A uniform air flow is injected upward from the bottom boundary. The slip boundary condition is used for gas flow at the side boundaries, and the convective outflow condition is used at the outlet boundary. A superficial velocity is used to realize $Re_s = 3000$. Here, Re_s is the sphere Reynolds number defined as

Table 1. Calculation Conditions

Gas		
Reynolds number: Re_s	−	3000
Superficial gas velocity: u_0 ($=Re_s\nu/d_s$)	m/s	1.13
Density: ρ_f	kg/m^3	1.205
Viscosity: μ_f	Pa s	1.81×10^{-5}
Particle		
Diameter: d_p	m	2.0×10^{-3}
Number of particles: N_p	−	483750
Initial bed height: H_i	m	0.15
Sphere		
Diameter: d_s	m	40.0×10^{-3}
Fictitious volume fraction: α_{fic}	−	0.74
Diameter of fictitious particle: d_{fic} ($=d_p/3$)	m	0.67×10^{-3}
Calculation		
Cell size: Δx, Δy, Δz	m	5.0×10^{-3}
Number of cell ($x \times y \times z$)	−	$30 \times 30 \times 120$
Time increment: Δt	s	1.0×10^{-5}

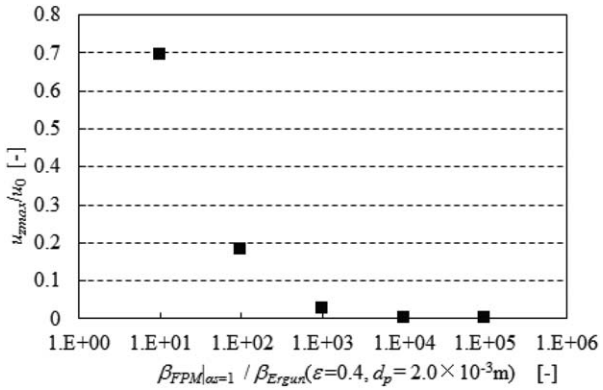

Figure 7. Maximum fluid velocity in the cells completely immersed in the sphere ($\alpha_s = 1$).

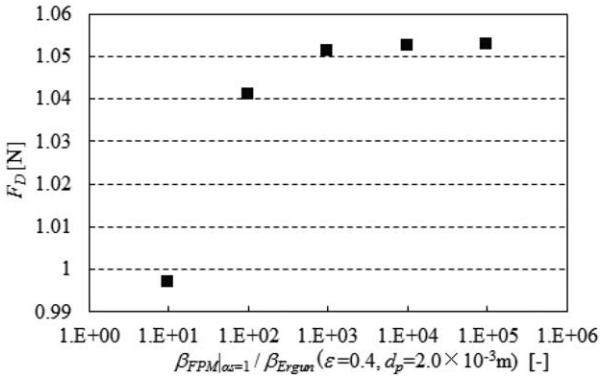

Figure 8. Fluid force acting on the sphere fixed in a packed bed.

Table 2. Calculation Conditions

Gas					
Sphere Reynolds number: Re_s	–	10		3000	
Superficial gas velocity: u_0 ($=Re_s\nu/d_s$)	m/s	3.76×10^{-3}		1.13	
Density: ρ_f	kg/m^3	1.205			
Viscosity: μ_f	Pa s	1.81×10^{-5}			
Particle					
Diameter: d_p	m	1.0×10^{-3}	2.0×10^{-3}		4.0×10^{-3}
Void ratio of particle layer	–	0.4			
Sphere					
Diameter: d_s	m	40×10^{-3}			
Fictitious volume fraction: α_{fic}	–	0.74			
Diameter of fictitious particle: d_{fic}	m	d_p	$d_p/3$	$d_p/2$	$d_p/10$
Calculation					
Resolution: $d_s/\Delta x$	–	4	8	16	32
Cell size: Δx	m	10.0×10^{-3}	5.00×10^{-3}	2.50×10^{-3}	1.25×10^{-3}
Number of cells ($x \times y \times z$)	–	$15 \times 15 \times 60$	$30 \times 30 \times 120$	$60 \times 60 \times 240$	$120 \times 120 \times 480$
Time increment: Δt	s	1.0×10^{-5}			

$$Re_s = \frac{u_0 d_s}{\nu} \tag{29}$$

where u_0 is the superficial velocity of the bed and d_s is the diameter of the sphere.

Gas tends to flow into areas with lower resistance, and flow penetration occurs, when the fluid resistance inside the sphere is not sufficiently large compared to the surrounding emulsion phase. We compare the flow penetration and fluid

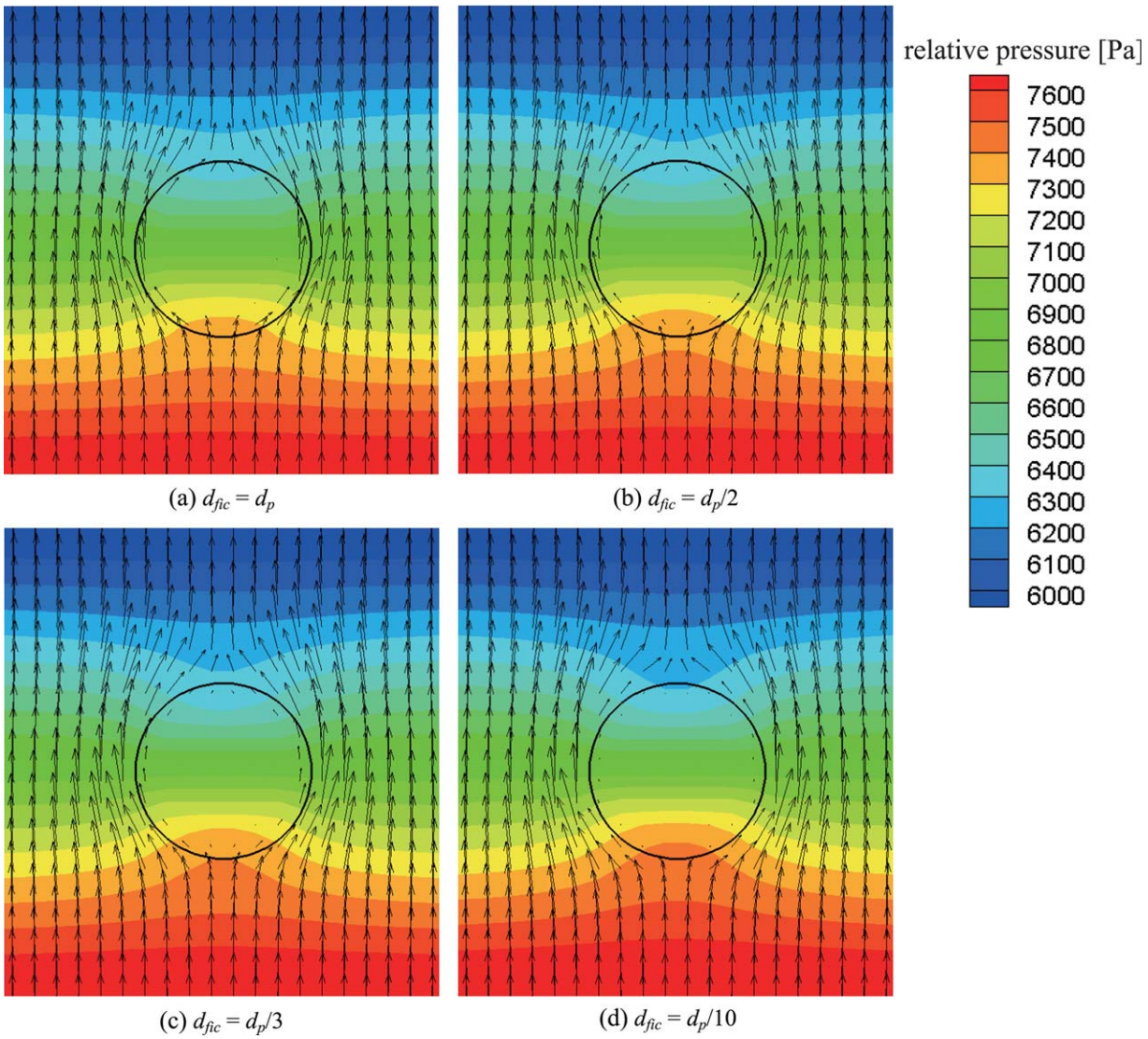

Figure 9. Averaged gas velocity and relative pressure distributions in a plane including the sphere center.

[Color figure can be viewed in the online issue, which is available at wileyonlinelibrary.com.]

Table 3. d_{fic} and F_d

d_{fic} (m)	d_p	$d_p/2$	$d_p/3$	$d_p/10$
F_D (N)	0.873	0.932	0.959	1.030

drag force working on the sphere for five cases by varying the magnitude of β_{FPM} for the cells completely immersed in the sphere: $\beta_{FPM}|_{\alpha_s=1}$. The cases have values that are 10, 10^2, 10^3, 10^4, and 10^5 times larger than $\beta_{Ergun}(\varepsilon, d)$, where $\beta_{Ergun}(\varepsilon, d)$ denotes the magnitude of β estimated from the Ergun equation with ε and d:

$$\beta_{Ergun} = \frac{\mu_f(1-\varepsilon)}{d^2\varepsilon}[150(1-\varepsilon)+1.75Re] \tag{30}$$

This is the estimation of β in the surrounding emulsion phase. The bulk void fraction of the packed bed in the above packing procedure is almost 0.4 and we adopt $\varepsilon = 0.4$. The particle size $d = d_p = 2.0 \times 10^{-3}$ m. The fictitious volume fraction and the diameter of fictitious particles in the cells including sphere surface are set to $\alpha_{fic} = 0.74$ and $d_{fic} = d_p/3$, respectively. Calculation conditions are shown in Table 1.

Figure 7 shows the relation between $\beta_{FPM}|_{\alpha_s=1}$ and the maximum gas velocity inside the sphere. The vertical axis shows the maximum gas velocity observed in the cells perfectly immersed in the sphere ($\alpha_s = 1$) u_{zmax}. Only the streamwise component is shown, and the results are normalized using u_0. Figure 8 shows the relation between $\beta_{FPM}|_{\alpha_s=1}$ and the fluid drag force working on the sphere F_D, which is obtained using Eq. 28. From Figures 7 and 8, it can be observed that the amount of gas penetration tends to be small as $\beta_{FPM}|_{\alpha_s=1}$ increases and, correspondingly, the fluid drag force approaches a certain value. Larger values realize the perfect solidity of a sphere body, but they also provoke numerical instabilities and necessitate small time increments. In this study, from the results in Figures 7 and 8, we adopt a magnitude 10^3 times larger than the surroundings in the cells with $\alpha_s = 1$. It is noted again that $\beta_{FPM}|_{\alpha_s=1}$ cannot be defined independently; rather, it should be defined relative to the fluid resistance in the surroundings. Accordingly, $\beta_{FPM}|_{\alpha_s=1}$ should be changed when the size of the surrounding particles changes.

Model parameters for cells including sphere surface ($0 < \alpha_s < 1$)

In this section, we consider model parameters for the cells including sphere surfaces shown with light gray in Figure 5. Investigations are performed in a packed bed and a sphere with $d_s = 40.0 \times 10^{-3}$ m is fixed at $x = 0.075$, $y = 0.075$, and $z = 0.200$ m. The same boundary condition with the previous section is used for the fluid flow. To perform

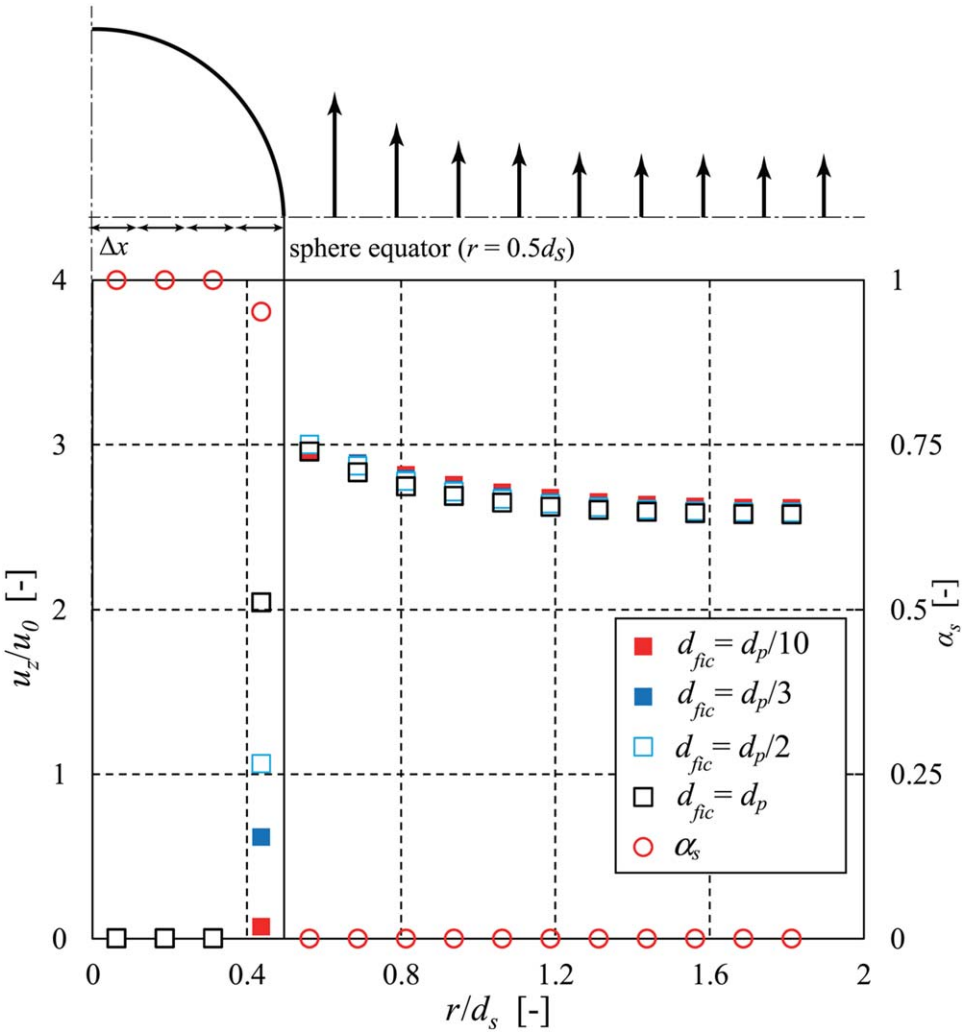

Figure 10. Distributions of u_z/u_0, and α_s at the sphere equator.

[Color figure can be viewed in the online issue, which is available at wileyonlinelibrary.com.]

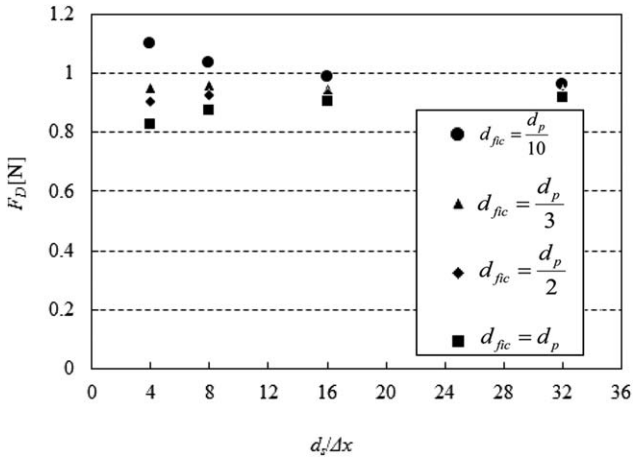

Figure 11. Dependency on spatial resolution ($Re_s = 3000$, $d_p = 2.0 \times 10^{-3}$ m).

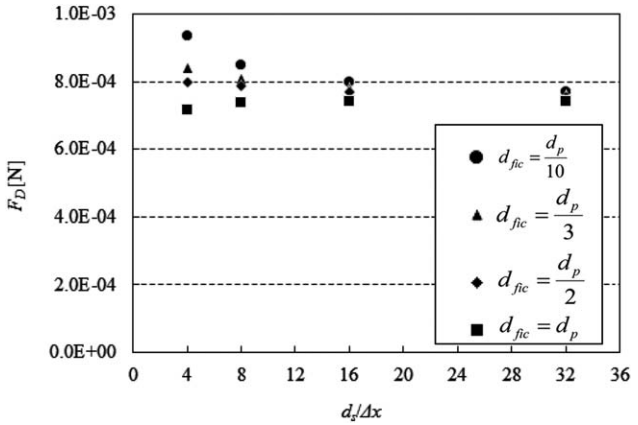

Figure 12. Dependency on spatial resolution ($Re_s = 10$, $d_p = 2.0 \times 10^{-3}$ m).

investigations under an ideal condition, the void fraction at each computational cell is directly defined by assuming that particles are packed homogeneously instead of packing particles actually. α_p is set to 0.6, where the existence of particles is expected.

It may be possible to determine two model parameters α_{fic} and d_{fic} individually, but this makes the procedure complex; to simplify the model parameter determination process, the fictitious volume fraction is fixed to $\alpha_{fic} = 0.74$ assuming a highly packed status inside the sphere, and we focus only on the size dependency of fictitious particles. Calculation conditions are shown in Table 2. In addition to the diameter of the fictitious particle, we also vary the spatial resolution of the calculations, the emulsion particle size, and the sphere Reynolds number.

Flows around a sphere depending on d_{fic}

To measure the change of flow field depending on d_{fic}, we observed the average gas flow fields around the fixed sphere. Here, four cases with different fictitious particle sizes, $d_{fic} = d_p$, $d_p/2$, $d_p/3$, and $d_p/10$, are compared. A uniform cell

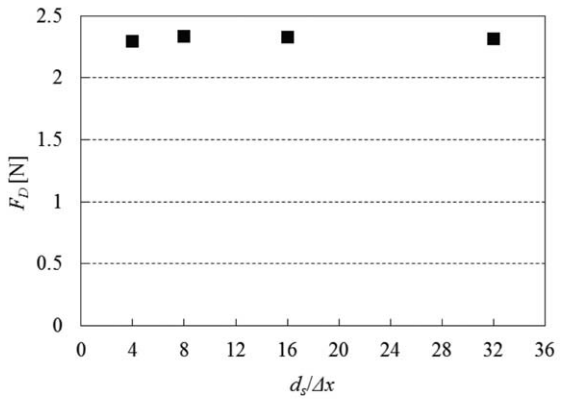

(a) $d_p = 1.0 \times 10^{-3}$ m, $Re_s = 3000$

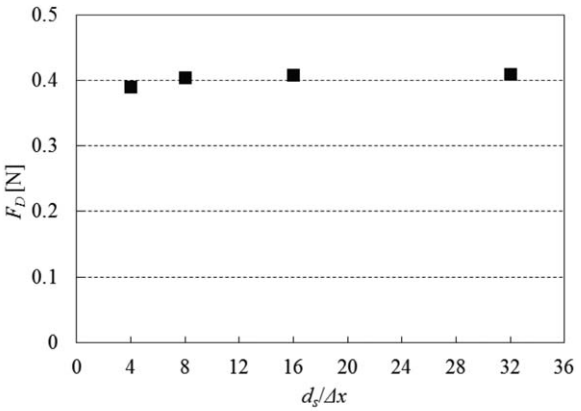

(b) $d_p = 4.0 \times 10^{-3}$ m, $Re_s = 3000$

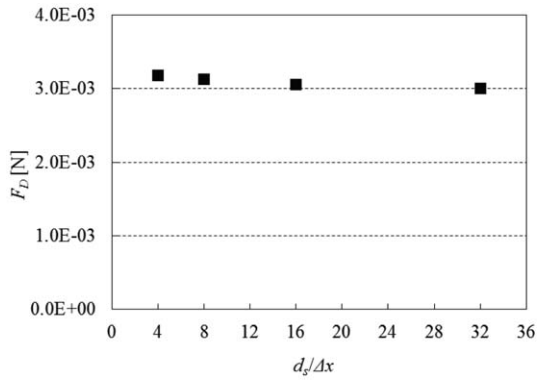

(c) $d_p = 1.0 \times 10^{-3}$ m, $Re_s = 10$

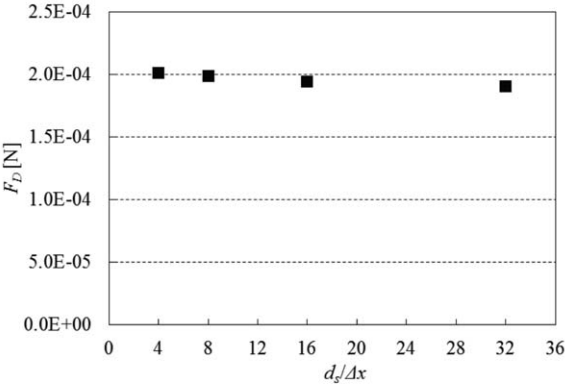

(d) $d_p = 4.0 \times 10^{-3}$m, $Re_s = 10$

Figure 13. Dependency on spatial resolution ($d_{fic} = d_p/2$).

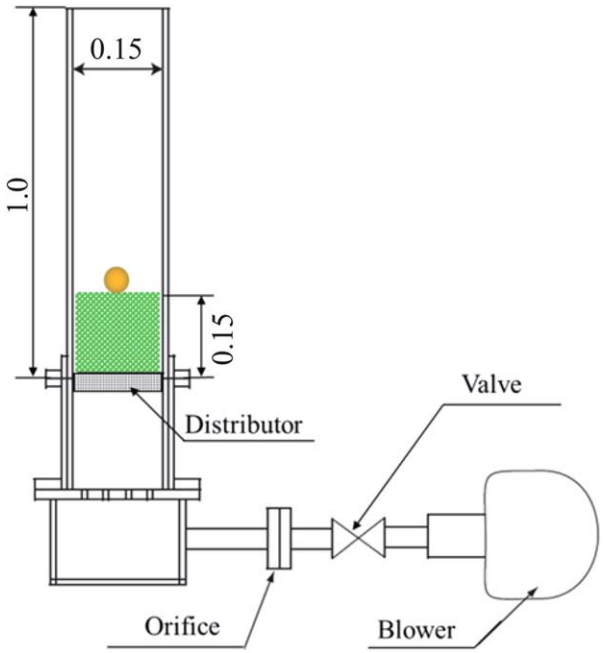

Figure 14. Experimental setup.

[Color figure can be viewed in the online issue, which is available at wileyonlinelibrary.com.]

size is used in this study, and spatial resolution is defined as the number of computational cells per sphere diameter ($d_s/\Delta x$). In this section, we use $d_s/\Delta x = 8$, $Re_s = 3000$, and $d_p = 2.0 \times 10^{-3}$ m. From the results in the previous section, $\beta_{FPM}|_{\alpha_s=1}$ is set to $10^3 \times \beta_{Ergun}$ ($\varepsilon = 0.4$, $d = 2.0 \times 10^{-3}$ m).

Figure 9 shows the average gas velocity and pressure distributions in a plane including the sphere center. It is obvious from the figures that the gas flows approaching from the bottom goes around the sphere in all cases. The velocity vectors near the surface existing inside the sphere are that of computational cells including the sphere surface. In the proposed model, the slip velocity of the cells including the sphere surface is allowed and larger slips are observed with larger d_{fic} as shown in Figure 9. Conversely, slip velocity is not confirmed in the cells completely immersed in the sphere ($\alpha_s = 1$). We also observe that the pressure distribution changes with d_{fic}. When a small d_{fic}, such as $d_p/10$, is used, the fluid resistance of the cells including the sphere surface becomes larger and tends to exclude the approaching gas flow to the sphere, resulting in a higher pressure gradient. The fluid drag force working on the sphere is shown in Table 3. As expected, the fluid drag force increases as the fictitious particle becomes smaller. Figure 10 shows the spanwise distributions of the averaged streamwise gas velocity and the solid volume fraction of the sphere at the sphere equator. The streamwise gas velocity is normalized by the superficial velocity. In the cells including sphere surface ($0 < \alpha_s < 1$), the streamwise gas velocity changes depending on the size of the fictitious particle corresponding to Figure 9. With a large fictitious particle, we can realize the large slip in the interface cells and vice versa.

Dependency on spatial resolution, sphere Reynolds number, and emulsion particle size

Figures 11 and 12 show the relation between spatial resolution and the fluid drag force at $Re_s = 3000$ and 10, respectively. d_p is fixed to 2.0×10^{-3} m throughout the comparisons. From the figures, we observed that the fluid drag force approaches a certain value regardless of the size of the fictitious particles in higher spatial resolutions. Conversely, the dependency on d_{fic} is observable in lower resolution cases. We expect that the effect of the cells including sphere surface becomes relatively less important when the resolution becomes higher. The magnitude of the fluid drag is different between two distinct Reynolds number cases, but similar behavior is observed in Figures 11 and 12. In the case of $d_{fic} = d_p/3$ and $d_p/2$, we still observe the difference depending on the resolution in the lowest resolution case; however, resolution dependency is not apparent as compared to the other cases throughout the region of comparison.

Results at different particle sizes, $d_p = 1.0 \times 10^{-3}$ and 4.0×10^{-3} m, where the fictitious particle size is fixed to $d_p/2$,

Table 4. Calculation Conditions for the Motion of A Single Sphere in A Bubbling Fluidized Bed

Particle and Sphere		
Particle diameter: d_p	m	2.3×10^{-3}
Number of particles: N_p	–	333775
Density of particle: ρ_p	kg/m^3	2500
Apparent density of particle bed: ρ_b	kg/m^3	1530
Initial bed height: H_i	m	0.15
Diameter of sphere: d_s	m	39.7×10^{-3}
Density of sphere: ρ_s	kg/m^3	1148, 1408, 1530, 1683, 1989, 2463
ρ_s/ρ_b	–	0.75, 0.92, 1.00, 1.10, 1.30, 1.61
Diameter of fictitious particle: d_{fic}	m	1.15×10^{-3} ($d_p/2$)
Fictitious volume fraction: α_{fic}	–	0.74
Normal spring constant: k_n	N/m	800
Tangential spring constant: k_t	N/m	200
Coefficient of restitution: e_p	–	0.9
Coefficient of friction: μ	–	0.5
Gas		
Superficial velocity: u_0	m/s	1.4
Viscosity: μ_f	Pa s	1.81×10^{-5}
Density: ρ_f	kg/m^3	1.205
Calculation		
Time increment: Δt	s	7.0×10^{-5}
Computational area: $L_x \times L_y \times L_z$	m	$0.15 \times 0.15 \times 0.60$
Cell size: Δx, Δy, Δz	m	5.56×10^{-3}
Ratio between sphere diameter and fluid cell: $d_s/\Delta x$	–	7.15

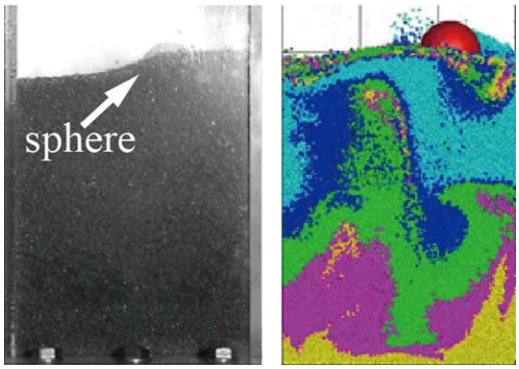

Figure 15. Snapshot of sphere and particles in $\rho_s/\rho_b = 0.75$ case.

[Color figure can be viewed in the online issue, which is available at wileyonlinelibrary.com.]

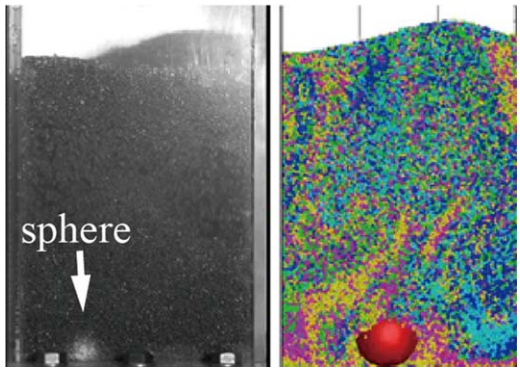

Figure 16. Snapshot of sphere and particles in $\rho_s/\rho_b = 1.61$ case.

[Color figure can be viewed in the online issue, which is available at wileyonlinelibrary.com.]

are shown in Figure 13, where the difference of the fluid drag force between the lowest ($d_s/\Delta x = 4$) and highest resolution ($d_s/\Delta x = 32$) is less than 5%. We conclude that, by using $d_{fic} = d_p/2$, the fluid drag force working on a sphere in ideal packed beds is most insensitive to the spatial resolution and similar to the nearly converged magnitude in the higher resolution case. Hereafter, we adopt $\alpha_{fic} = 0.74$ and $d_{fic} = d_p/2$ as model parameters in the cells including sphere surface.

Motion of a Single Sphere in a Bubbling Fluidized Bed

Experimental and calculation conditions

We perform a validation study of the proposed model for the motion of a large sphere in a 3-D bubbling fluidized bed. Our experimental setup is shown in Figure 14. The fluidized bed has dimensions of 0.15 m depth, 0.15 m width, and 1.00 m height. We use 2.3×10^{-3} m spherical glass particles and set the initial bed height to 0.15 m. We add a single hollow sphere of diameter 39.7×10^{-3} m to the bed, which is 17.26 times larger than the glass particles. The density of the sphere is adjusted by filling it with a given amount of the mixture of small glass particles and solder chips inside the sphere. Air at room temperature is injected uniformly into the bed from the bottom. In the present condition, the minimum fluidization velocity is $u_{mf} = 1.0$ m/s. We set the superficial velocity to $u_0 = 1.4$ m/s and observe six spheres with different densities, 1148, 1408, 1530, 1683, 1989, and 2463 kg/m^3, to determine the sphere motion.

Calculation conditions are shown in Table 4. *x*, *y*, and *z* show the depth, width, and height directions, respectively. After locating a sphere at the center of the bed surface, we start the gas injections. In this study, from the results of former sections, we adopt $d_{fic} = d_p/2$, $\alpha_{fic} = 0.74$, and $\beta_{FPM}|_{\alpha_s = 1} = 10^3 \times \beta_{Ergun}$ ($\varepsilon = 0.4$, $d = d_p$).

Motion of a single sphere

Snapshots of the experiment and the calculation results appear in Figures 15–17. Only the results with $\rho_s = 1148$, 1530, and 2463 kg/m^3 are shown here. The density of the sphere is normalized using the apparent density of the bed before fluidization started, $\rho_b = 1530$ kg/m^3. The observations in the experiments are from the bed front while the calculations are performed with respect to the bed center. Only for the case in which $\rho_s/\rho_b = 1.00$ (Figure 17), the temporal development of the sphere and particle motion is shown.

Fluidization and the formation of bubbles are confirmed in all cases. In the $\rho_s/\rho_b = 0.75$ case (Figure 15), the sphere cannot penetrate the particle bed and stays near the free surface of the particle layer. In the $\rho_s/\rho_b = 1.61$ case (Figure 16), on the other hand, the sphere sinks to the bed bottom immediately after the fluidization has started and stays near the bottom wall. In the $\rho_s/\rho_b = 1.00$ case (Figure 17), the sphere descends through the particle bed slightly and repeats upward and downward motions corresponding to the motion of the bubbles spontaneously formed in the bed. This behavior is observed both in the experiment and the model calculation. Figure 18 shows the calculation results of the sphere's vertical position normalized by the initial bed height. Upward and downward motions of the sphere are confirmable except in the $\rho_s/\rho_b = 1.61$ case. In Figure 17, the sphere exists in the bed between 0.20 and 0.30 s, while it is visually inaccessible due to the existence of dense particles in the experiment.

It is difficult to validate the proposed model only from the snapshots shown in Figures 15–17 and so quantitative comparisons are also performed. Figure 19 shows the stable vertical positions of the spheres after the gas injection has stopped. The vertical center position of the spheres is normalized by the initial bed height. The measurement of sphere positions is performed after the solids have fully settled. Both experiments and calculations are repeated five times for each case, and the averages are shown with their standard deviations. As shown in Figure 19, we have confirmed that the proposed model reproduces the experimental results well especially in the regimes $\rho_s/\rho_b \leq 0.92$ and $\rho_s/\rho_b \geq 1.61$. We have observed that the standard deviation becomes large when ρ_s/ρ_b approaches 1.1. The sphere is easily transported by the local flows induced by bubbles, when ρ_s approaches ρ_b and the stable vertical position of the sphere varies greatly depending on the state when the gas injection is stopped. As in the experimental result, we observed a large standard deviation in the calculation for the $\rho_s/\rho_b = 1.1$ case. The average and standard deviation show slightly different values between the experiment and the calculation and further investigations are needed.

Forces working on a sphere and local flow structures

Calculations using the proposed model enable the discussion on the relation between the sphere motion and the forces working on a sphere in detail. In this section, we

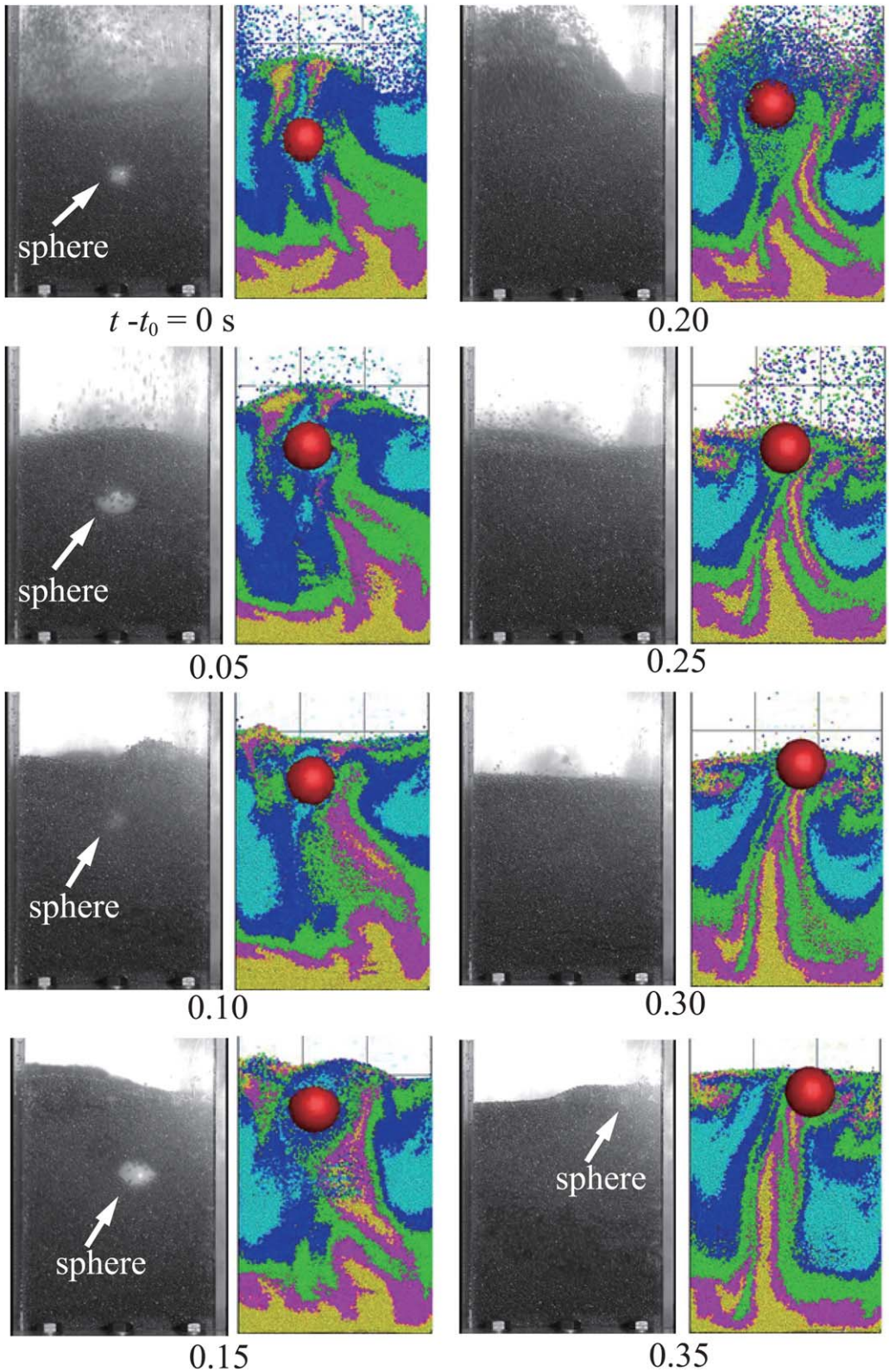

Figure 17. Snapshots of sphere and particles in $\rho_s/\rho_b = 1.00$ case.

[Color figure can be viewed in the online issue, which is available at wileyonlinelibrary.com.]

show the result of the $\rho_s/\rho_b = 1.0$ case. Figure 20 is the time-history of (a) sphere center position, (b) translational velocity, (c) total force working on the sphere, and (d) force components. Only vertical (z) components are shown here. The forces working on the sphere are due to the fluid F_{Fz}, the contacts F_{Cz}, and the gravity F_G and these are shown separately in Figure 20d. The center position, the velocity, and the forces are normalized by the initial bed height, the superficial velocity, and the magnitude of gravity, respectively. From Figure 20a, we observe that the sphere repeats upward and downward motions fairly regularly during fluidization. To develop discussion in more detail, we focus on a

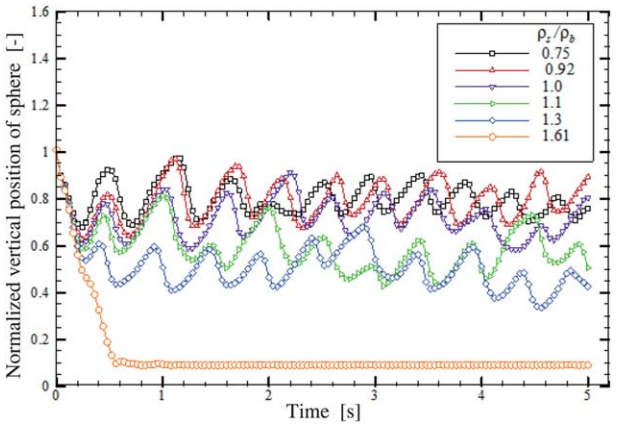

Figure 18. Normalized vertical position of sphere center.

[Color figure can be viewed in the online issue, which is available at wileyonlinelibrary.com.]

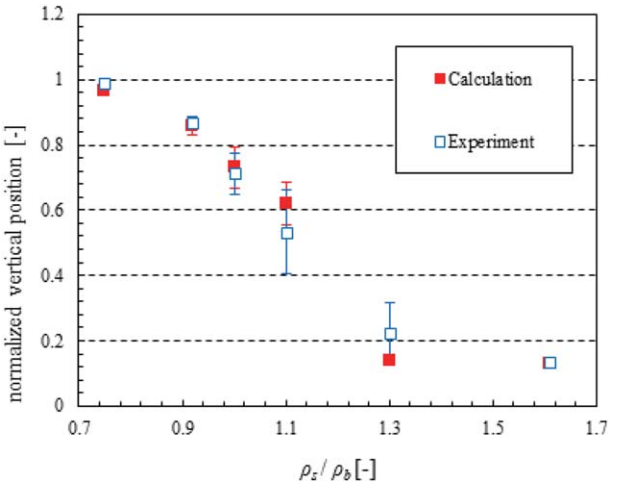

Figure 19. Stable vertical position of sphere after fluidization has stopped.

[Color figure can be viewed in the online issue, which is available at wileyonlinelibrary.com.]

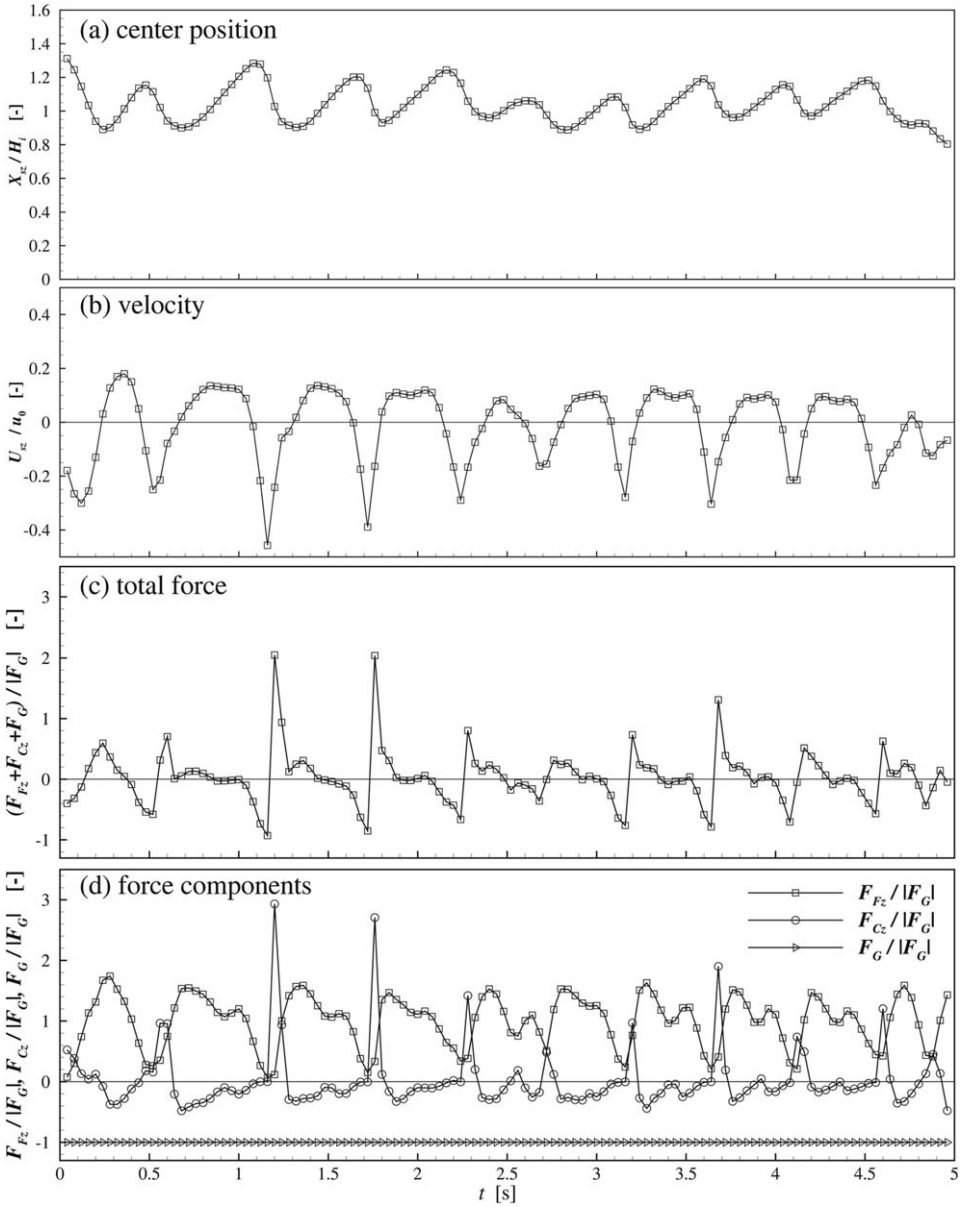

Figure 20. Vertical position, velocity, and forces in $\rho_s/\rho_b = 1.00$ case.

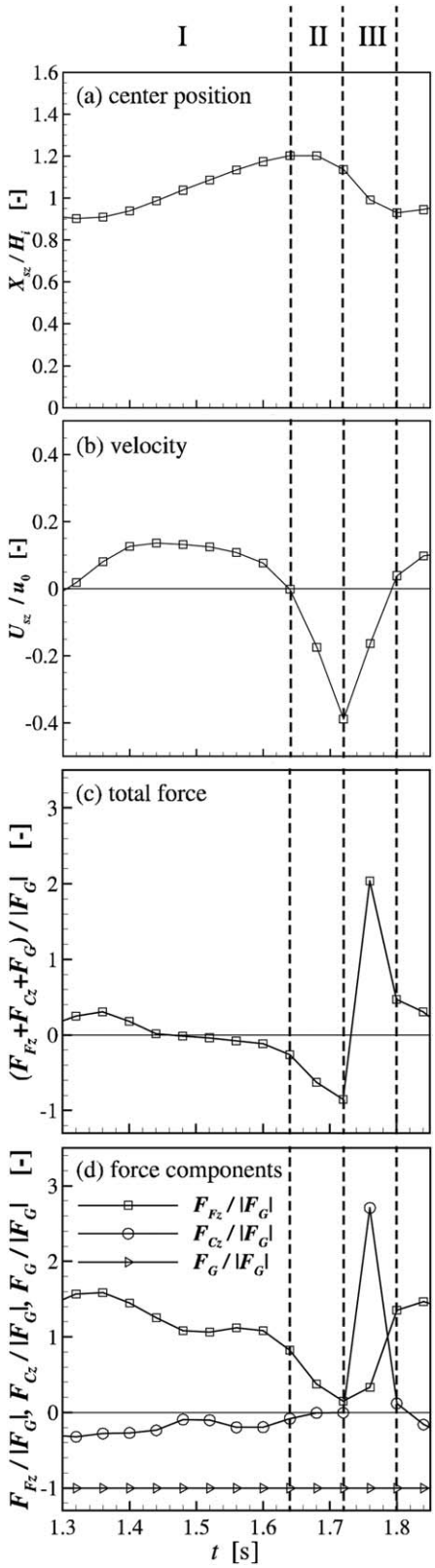

Figure 21. Vertical position, velocity, and forces between 1.30 and 1.85 sec in $\rho_s/\rho_b = 1.00$ case.

period which includes a typical sequence of upward and downward motions of the sphere. Figure 21 shows the results between 1.30 and 1.85 s. Generally, the sequence can be divided into three stages I–III as depicted in Figure 21.

In the stage I ($1.30 < t \leq 1.64$ s), which is characterized by the positive vertical velocity, the sphere is elevated. From Figure 21d, it is confirmed that this is due to the positive fluid force. We also know that the contact force during the stage is negative and only works as a resistance to the sphere. In the upcoming stage II ($1.64 < t \leq 1.72$ s), the sphere turns to downward motion. The fluid force decreases rapidly and a large negative force is working on the sphere as a total. It is interesting that the contact force working as a resistance in the stage I also decreases during this stage. At 1.72 s, the fluid and the contact force almost disappear and only the gravity force is working on the sphere. In the stage III ($1.72 < t \leq 1.80$ s), an impulsive positive contact force which prevents the downward motion of the sphere is observed. Finally, the recovery of positive fluid and negative contact forces that were observed in the stage I is confirmed after 1.80 s. From Figure 20, we can confirm that similar processes characterized by the stage I–III are repeated during fluidization.

The results of corresponding void structure visualization are shown in Figure 22, where $\varepsilon = 0.8$ isosurface is depicted. A and B at 1.52 s are the free surface of the particle bed and the bubble generated at the bed bottom, respectively. At 1.60 s, close to the end of stage I, the generation of a new bubble under the sphere is confirmed (C). Bubble development from the bottom of an immersed object in fluidized beds has been reported in a number of studies.[27–31] The bubble generated under the sphere grows larger as D after 1.60 s. The downward motion of the sphere in the stages II and III is due to the sphere penetrating the bubble observed between 1.64 and 1.76 s. In an emulsion phase, a large pressure drop occurs in the streamwise direction due to the existence of dense particles and the streamwise pressure gradient around the sphere works as a pressure drag force. Inside of the bubble such as that observed in 1.72 s, conversely, the pressure gradient almost disappears. Moreover, the chance of contact with particles decreases inside of the bubble and the gravity force becomes a dominant as observed in Figure 21. As a result of penetration, the sphere surface reaches the end of bubble surface at 1.76 s (E). The impulsive contact force in the stage III is due to the contacts with dense emulsion particles; the sphere experiences contact during the reentry to dense emulsion phase. After 1.80 s, the sphere stays in a dense emulsion phase and positive fluid and negative contact forces are recovered.

As we demonstrated here, the upward and downward motions of the $\rho_s/\rho_b = 1.0$ sphere are largely influenced by the bubble generated near the sphere. It is emphasized that the size of the generated bubble is comparable to the sphere and it is difficult to capture such phenomenon by conventional DEM–CFD models. This study is restricted to a single sphere; however, it suggests the importance of direct interactions between large solids and bubbles, when we consider the behavior of binary systems with large size differences. The discussion in this section is purely numerical and further experimental explorations are also needed.

Conclusions

In this article, we proposed a new numerical model that can predict and reproduce the motion of flows including dense solids with large size differences. The model is based on the DEM–CFD model and the VP method. It combines the mesoscopic model for small solids and the direct

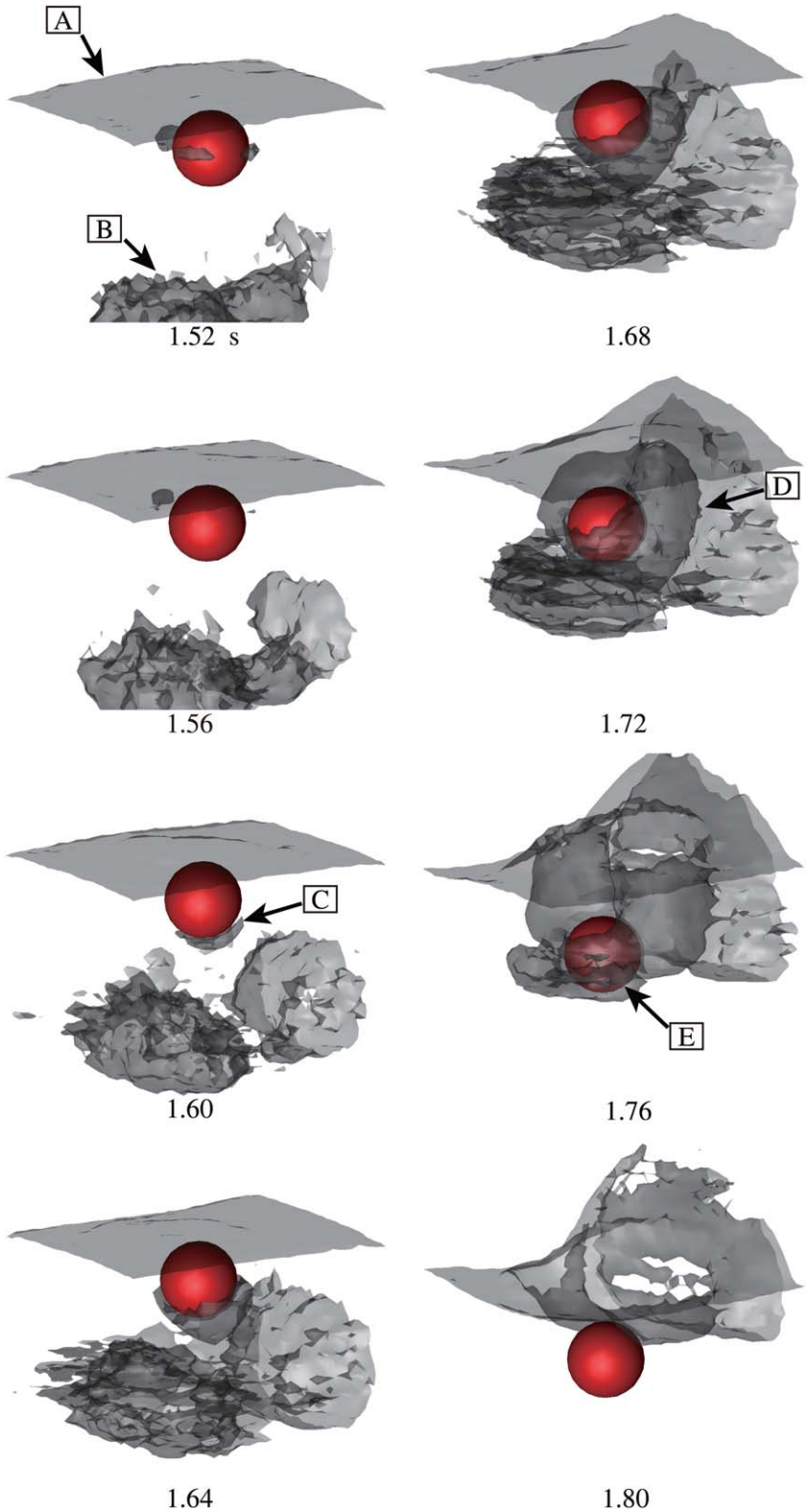

Figure 22. Void structure visualization in $\rho_s/\rho_b = 1.00$ case ($\varepsilon = 0.80$ isosurface is shown).

[Color figure can be viewed in the online issue, which is available at wileyonlinelibrary.com.]

simulation for large solids, representing phenomena at different scales, in a unified manner. The amount of momentum exchange between the fluid and solids was estimated by assuming that a large solid consists of dense small fictitious particles. There is no need, in practice, to replace the large solid with fictitious particles, and hence, we can avoid excessive computer resources for representing each fictitious particle. It is easy to add the proposed model to the software based on DEM–CFD models.

Ergun and Wen and Yu equations (Eqs. 10 and 11) have been used as drag correlations in this study; however, this is not mandatory, and a number of other options are selectable.

Two model parameters, the fictitious particles size and the fictitious volume fraction, have been introduced. It is possible to control these two parameters independently; however, it makes the calibration procedure complex and only the fictitious particle size is used as an adjusting parameter in this study. Through the number of parameter dependency studies, we found the model parameters $d_{\mathrm{fic}} = d_{\mathrm{p}}/2$, $\alpha_{\mathrm{fic}} = 0.74$, and $\beta_{\mathrm{FPM}}|_{\alpha_{\mathrm{s}}=1} = 10^3 \times \beta_{\mathrm{Ergun}}(\varepsilon = 0.4, d = d_{\mathrm{p}})$.

Validation studies of the proposed model have been performed qualitatively and quantitatively for the motion of a sphere in a bubbling fluidized bed. After the fluidization has stopped, we compared the motion and the stable vertical position of the spheres of the calculations with those of the experiment. The present numerical model shows good predictions especially when the density of the sphere is relatively large or small compared to the apparent density of the bed.

Calculations using the proposed model enable detailed discussion on the relation between sphere motions, forces, and local flow structures around the sphere. The bubble development from the sphere bottom was observed for the $\rho_{\mathrm{s}}/\rho_{\mathrm{b}} = 1.0$ case and the importance of direct interactions between the sphere and the bubble, which are difficult to observe with conventional DEM–CFD models, was suggested.

The proposed model can express the slip velocity at the cells including sphere surface, and its amount is controllable by the parameter d_{fic} as observed in Figures 9 and 10. In the mesoscopic models based on averaged equations, this is still an open question; it is not proper to use the no-slip boundary condition at solid walls; some slip should be allowed.[32,33] The model can be applicable to an external boundary and will be a good tool to show slips at the cells including solid walls.

Acknowledgments

The authors greatly appreciate Jun Oshitani, Mikio Yoshida, and Yusumi Nagahashi for their helpful discussion. A part of this study was supported by Hosokawa Powder Technology Foundation, the Ministry of Education, Culture, Sports, Science, and Technology (MEXT): "Strategic programs for innovative research (SPIRE)–research field No. 4: industrial innovations" and Grant-in-Aid for Scientific Research (C), JSPS KAKENHI Grant No. 25420122. Their supports are greatly appreciated.

Literature Cited

1. Oshitani J, Ono K, Ijiri M, Tanaka Z. Effect of particle fluidization intensity on floating and sinking of objects in a gas-solid fluidized bed. *Adv Powder Technol*. 2004;15(2):201–213.
2. Oshitani J, Kawahito T, Yoshida M, Gotoh K, Franks GV. The influence of the density of a gas-solid fluidized bed on the dry dense medium separation of lump iron ore. *Miner Eng*. 2011;24(1):70–76.
3. Reynoldson RW. *Heat Treatment in Fluidized Bed Furnaces*. Material Park, OH: ASM International, 1993.
4. Rahmanian N, Ghadiri M, Jia X. Seeded granulation. *Powder Technol*. 2011;206(1–2):53–62.
5. Tsuji Y, Kawaguchi T, Tanaka T. Discrete particle simulation of 2-dimensional fluidized-bed. *Powder Technol*. 1993;77(1):79–87.
6. Xu BH, Yu AB. Numerical simulation of the gas-solid flow in a fluidized bed by combining discrete particle method with computational fluid dynamics. *Chem Eng Sci*. 1997;52(16):2785–2809.
7. Feng YQ, Yu AB. Effect of bed thickness on the segregation behavior of particle mixtures in a gas fluidized bed. *Ind Eng Chem Res*. 2010;49(7):3459–3468.
8. Wang SY, Lu HL, Li X, Wang JZ, Zhao YH, Ding YL. Discrete particle simulations for flow of binary particle mixture in a bubbling fluidized bed with a transport energy weighted averaging scheme. *Chem Eng Sci*. 2009;64(8):1707–1718.
9. Beetstra R, van der Hoef MA, Kuipers JAM. Numerical study of segregation using a new drag force correlation for polydisperse systems derived from lattice-Boltzmann simulations. *Chem Eng Sci*. 2007;62(1–2):246–255.
10. Bokkers GA, Annaland MVS, Kuipers JAM. Mixing and segregation in a bidisperse gas-solid fluidised bed: a numerical and experimental study. *Powder Technol*. 2004;140(3):176–186.
11. Hoomans BPB, Kuipers JAM, van Swaaij WPM. Granular dynamics simulation of segregation phenomena in bubbling gas-fluidised beds. *Powder Technol*. 2000;109(1–3):41–48.
12. Feng YQ, Xu BH, Zhang SJ, Yu AB, Zulli P. Discrete particle simulation of gas fluidization of particle mixtures. *AIChE J*. 2004;50(8):1713–1728.
13. Rong DG, Mikami T, Horio M. Particle and bubble movements around tubes immersed in fluidized beds: a numerical study. *Chem Eng Sci*. 1999;54(23):5737–5754.
14. Wu CL, Zhan JM, Li YS, Lam KS. Dense particulate flow model on unstructured mesh. *Chem Eng Sci*. 2006;61(17):5726–5741.
15. Liu DY, Bu CS, Chen XP. Development and test of CFD-DEM model for complex geometry: a coupling algorithm for Fluent and DEM. *Comput Chem Eng*. 2013;58:260–268.
16. Guo Y, Wu CY, Thornton C. Modeling gas-particle two-phase flows with complex and moving boundaries using DEM-CFD with an immersed boundary method. *AIChE J*. 2013;59(4):1075–1087.
17. Takeuchi S, Wang S, Rhodes M. Discrete element method simulation of three-dimensional conical-base spouted beds. *Powder Technol*. 2008;184(2):141–150.
18. Dietiker J-F, Li T, Garg R, Shahnam M. Cartesian grid simulations of gase-dimensional conical-base spouted beds. *Powder Technol*. 2013;235:696–705.
19. Kolomenskiy D, Schneider K. A Fourier spectral method for the Navier-Stokes equations with volume penalization for moving solid obstacles. *J Comput Phys*. 2009;228(16):5687–5709.
20. Schneider K. Numerical simulation of the transient flow behaviour in chemical reactors using a penalisation method. *Comput Fluids*. 2005;34(10):1223–1238.
21. Anderson TB, Jackson R. A fluid mechanical description of fluidized beds. *Ind Eng Chem Fundam*. 1967;6(4):527–539.
22. Ergun S. Fluid flow through packed columns. *Chem Eng Prog*. 1952;48(2):89–94.
23. Wen CY, Yu YH. Mechanics of fluidization. *Chem Eng Prog Symp Ser*. 1966;62(62):100–111.
24. Schiller VL, Naumann A. Uber die grundlegenden berechnungen bei der schwerkraftaufbereitung. *Z. Verenines Deutscher Inge*. 1933;77:318–321.
25. Tsuji T, Narutomi R, Yokomine T, Ebara S, Shimizu A. Unsteady three-dimensional simulation of interactions between flow and two particles. *Int J Multiphase Flow*. 2003;29(9):1431–1450.
26. Tsuji T, Yabumoto K, Tanaka T. Spontaneous structures in three-dimensional bubbling gas-fluidized bed by parallel DEM-CFD coupling simulation. *Powder Technol*. 2008;184(2):132–140.
27. Glass DH, Harrison D. Flow patterns near a solid obstacle in a fluidized bed. *Chem Eng Sci*. 1964;19:1001–1002.
28. Loew O, Shmutter B, Resnick W. Particle and bubble behaviour and velocities in a large-particle fluidized bed with immersed obstacles. *Powder Technol*. 1979;22(1):45–57.
29. Bouillard JX, Lyczkowski RW, Gidaspow D. Porosity distributions in a fluidized bed with an immersed obstacle. *AIChE J*. 1989;35:908–922.
30. Kim SW, Ahn JY, Kim SD, Hyun Lee D. Heat transfer and bubble characteristics in a fluidized bed with immersed horizontal tube bundle. *Int J Heat Mass Transf*. 2003;46(3):399–409.
31. Schmidt A, Renz U. Numerical prediction of heat transfer between a bubbling fluidized bed and an immersed tube bundle. *Heat Mass Transf*. 2005;41:257–270.
32. Beetstra R, van der Hoef MA, Kuipers JAM. Drag force of intermediate Reynolds number flow past mono- and bidisperse arrays of spheres. *AIChE J*. 2007;53(2):489–501.
33. Tsuji T, Narita E, Tanaka T. Effect of a wall on flow with dense particles. *Adv Powder Technol*. 2013;24(2):565–574.

Manuscript received Sep. 17, 2013, and revision received Dec. 6, 2013.